An Examination of Trapped Bubbles for Viscous Drag Reduction on Submerged Surfaces

Kelly A. Stephani
e-mail: kelly.stephani@mail.utexas.edu

David B. Goldstein
e-mail: david@cfdlab.ae.utexas.edu

Department of Aerospace Engineering and Engineering Mechanics,
University of Texas at Austin,
1 University Station,
C0600 Austin, TX 78712-0235

Viscous drag reduction on a submerged surface can be obtained both in the limit of an unbroken gas film coating the solid and in the nanobubble or perhaps microbubble coating regime when an air layer is created with superhydrophobic coatings. We examine an intermediate bubble size regime with a trapped-bubble array (TBA) formed in a tap water environment using electrolysis to grow and maintain bubbles in thousands of millimeter-sized holes on a solid surface. We show that even though surface tension is sufficient to stabilize bubbles in a TBA against hydrostatic and shear forces beneath a turbulent boundary layer, no drag reduction is obtained. Drag measurements were acquired over Reynolds numbers based on plate length ranging from $7.2\times10^4<Re_L<3.1\times10^5$ *using either a force balance for plates mounted in a vertical orientation, or by performing a momentum integral balance using a wake survey for a flat plate mounted in either vertical or horizontal orientation. In that the drag forces were small, emphasis was placed on minimizing experimental uncertainty. For comparison, the flow over a flat plate covered on one side by a large uninterrupted gas film was examined and found to produce large drag reductions of up to 32%.* [DOI: 10.1115/1.4001273]

1 Introduction

1.1 Motivation and Background. The efficiency of a system involving submerged surfaces is often dependent on its ability to overcome viscous drag effects that are inherent to solid surface-liquid interaction. Drag reduction methods involving changes to the near-wall boundary condition have been investigated over a wide range of applications, from Poiseuille-flow and Stokes-flow problems (e.g., "lab-on-a-chip" technology) to high-speed underwater projectiles where Reynolds numbers are large and flow cavitation is possible. Implementation of these drag reduction methods also varies from passive surface textures to active systems, which require continuous energy expenditure to provide drag reduction.

The idea of using air injection to create an air film along the bottom of ship hulls and similar submerged surfaces has been of interest since the late 1800s. Successful implementation of this technique requires the generation of a stable air film on the hull bottom using a low air injection rate, which can be difficult to achieve without a thorough understanding of the physical mechanisms involved. Matveev [1] discusses some of the limiting parameters involved in artificial cavitation for air cavity ships. Latorre [2] provides a brief review examining the effectiveness of this application for high-speed planning craft as well as barges and cargo ships. While integration of the air injector system into the hull bottom creates appendage drag, using an appropriate air injection rate leads to a net decrease in the original base hull drag of 15–18% in model tests and 10–12% for full-scale applications. Overall, this drag reduction technique has demonstrated a reduction in the vehicle's net power requirement.

Drag reduction schemes involving microbubble injection into turbulent boundary layers by Madavan et al. [3,4], Pal et al. [5] and more recent work by Sanders et al. [6] have been shown to reduce friction. It is thought that although the addition of bubbles to a liquid effectively increases its viscosity, the bubbles act to reduce the liquid density and modify turbulence in the boundary layer so as to reduce skin friction. Sanders et al. [6] emphasize that microbubbles should be sized on the order of the smallest turbulent flow scales and remain within 300 wall units of the surface to be most effective. They also determined, in agreement with prior work, that for bubbles injected into the flow on the bottom side of the model surface, an increase in flow speed reduces the amount of drag reduction observed, with the maximum drag reduction occurring at the lowest test speed. This group was, in particular, able to demonstrate a sustained drag reduction over the length of the test plate for the lowest flow speeds studied ($6\ \mathrm{m\ s^{-1}}$). At these flow speeds, the bubbles injected into the flow through the upstream injector coalesced at the plate surface to form a quasi-continuous gas film, particularly at high gas injection rates, and reductions in local shear stress of up to nearly 100% were indicated on the bottom surface of the test plate. Similar to the microbubble injection drag reduction method, the method described in the present paper also utilizes tiny bubbles to reduce viscous drag; however, it is important to note that the drag reduction mechanism pursued here is quite different from bubble injection.

Some passive drag reduction methods (in which the flow conditions at the wall are modified using microfabrication techniques) have been investigated and show promising results. Balasubramanian et al. [7] investigated water flow over submerged hydrophobic surfaces and were able to demonstrate 10–20% viscous drag reduction. This benefit, however, diminished over time due to water infiltration of the air layer between the nanostructures on the surface. Velocity slip has been clearly measured over superhydrophobic or ultrahydrophobic surfaces at a microscale. Joseph et al. [8] measured slip in a water flow over a carbon nanotube forest on one wall of a microchannel. Gas between the nanotubes presumably kept the water confined to the forest canopy. Several microns of slip length were possible in distilled water provided the water did not infiltrate between the nanotubes. Ou et al. [9] used microparticle image velocimetry to measure large velocity slip in water

Contributed by the Fluids Engineering Division of ASME for publication in the JOURNAL OF FLUIDS ENGINEERING. Manuscript received June 27, 2008; final manuscript received February 9, 2010; published online April 20, 2010. Assoc. Editor: Steven Ceccio.

flow over a slotted silicon surface treated with a hydrophobic coating that prevented the liquid from penetrating into the slots. Laminar computational simulations of the arrangement were used as validation for the velocity measurements and showed good agreement with the gas bubble slip model. Pressure drop measurements through a channel demonstrated reduced viscous drag. Larger scale grooves containing gas have been examined [10] but the bubble films were found to be unstable in a shear flow and required continuous gas injection.

Hydrophobic surfaces show promise as a method for reducing drag on submerged surfaces. However, the limitations of the hydrophobic surface drag reduction methods, particularly loss of hydrophobicity over time or the small slip lengths obtained, suggest the need for a drag reduction method, which can produce a slip surface similar to that of a hydrophobic surface, but maintain a gas layer at the wall for extended periods of time. The method examined in this investigation accomplishes this by using electrolysis to form a layer of air on the submerged surface. Doing so could provide continuous drag reduction over perhaps any length of time desired with only small energy expenditures required to replace occasional bubble loss.

Ideally, an entire submerged surface would be covered in one large continuous bubble film, forming a near-slip surface and providing a drastic reduction in viscous drag. This, however, is not practical as a large bubble is easily torn away from the surface when subjected to high shear and buoyancy effects. As an alternative, it is suggested that covering the surface with millions of tiny, densely packed bubbles, which form a trapped-bubble array may provide nearly the same drag-reducing effects as one large, continuous bubble, while keeping the bubbles sufficiently small to remain attached to the submerged surface. Thus, in forming a TBA on a submerged surface, the bubble surface effectively replaces the solid surface it forms on, and therefore, the net shear stress on the entire surface should be reduced.

The bubbles in our TBA are produced by means of electrolysis. The TBA surface is selected as the cathode, so hydrogen gas is collected to form the trapped bubbles. Drag measurements are obtained over a range of Reynolds numbers for flow over a flat plate surface, a flat plate with a large trapped bubble, and a flat plate covered with the TBA using either a calibrated force balance system or by performing a momentum integral balance with a wake survey.

The remainder of this paper is divided as follows: Implementation of the bubble formation process as well as a description of the experimental facilities and apparatus follows directly from previous work by Stephani and co-workers [11,12] and will be discussed in the next section (Sec. 2). Results are presented and discussed in Sec. 3, followed by conclusions in Sec. 4. The objectives of this paper are to determine the effects of trapped bubbles on viscous drag by examining the net change in drag produced by the bubbles, as well as the mechanisms by which the bubbles may reduce drag. Since it is difficult to observe physical phenomena on the tiny trapped bubbles, we examine a single, large trapped bubble to investigate effects of contamination on bubble drag reduction, which we expect to apply to the tiny trapped bubbles. The large trapped bubble also demonstrates the maximum drag reduction that we may expect to obtain if the entire solid surface were covered with trapped bubbles. We emphasize that this research aims to investigate a potentially practical approach to drag reduction using the TBA [13]. The experiments are designed to emulate, in part, the environment in which this drag reduction method may be used, rather than study a computationally perfect model or a physical model that is useful only in near-pristine laboratory environments; the intention was to demonstrate an efficient drag reduction method. Thus, the bubbles are formed beneath a turbulent boundary layer developing over a flat plate with a vertical orientation such that the bubbles are not hydrostatically stabilized, and the experiments are performed in ordinary tap water that has received algicidal chemical treatment.

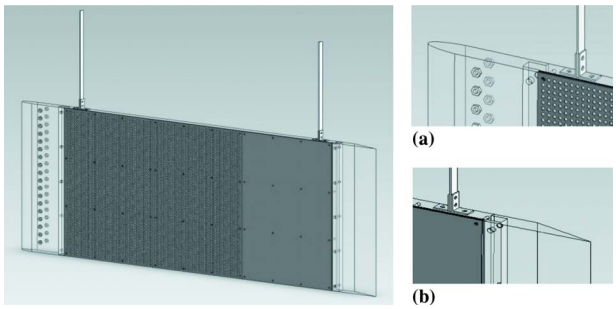

Fig. 1 Schematic of flat acrylic test plate assembly in vertical orientation with dark gray bubble plate inserts and thin flexures: (*a*) detailed view of the elliptical leading edge and (*b*) detailed view of the tapered trailing edge

2 Experimental Facilities and Apparatus

2.1 Water Channel Facility. All experiments in this study were conducted in an Eidetics model 1520 closed-loop water channel containing tap water. Flow velocity measurements are taken with a Dantec Dynamics BSA F50 two-component laser Doppler anemometer (LDA). Flow uniformity, even at the maximum speed of 0.4 m s^{-1}, is excellent. Horizontal and vertical velocity profiles were acquired throughout the test section with the LDA. Spanwise and vertical variation in the mean flow velocity was found to be less than 1% everywhere outside of the boundary layers, and variation in the centerline flow velocity along the length of the empty test section was at most 1%. LDA velocity measurements across the span of the test plate indicate that disturbances due to plate end effects start at the front of the plate and spread toward the plate centerline at a streamwise spreading angle of approximately 11 deg. Maximum freestream turbulence levels (represented as U'/U_∞) were found to be between 1–1.5% of the freestream velocity value anywhere in the test section outside the boundary layers over the entire useful range of water tunnel speeds. Water temperatures in the channel during experiments were observed to remain within $20.9\,^\circ\mathrm{C} \pm 0.3\,^\circ\mathrm{C}$, which corresponds to a nominal viscosity of 0.98 mPa s $\pm 0.75\%$.

2.2 Force Balance, Test Plate, and Components. The test plate used in this study is an adaptation of an earlier design [11,12] with several changes made to improve the plate's structural integrity and versatility. The 1.016 m $\times$ 0.381 m $\times$ 2.3 cm test plate is assembled from three interlocking pieces (Figs. 1(*a*) and 1(*b*)). The leading edge (Fig. 1(*a*)) has a 4:1 elliptical shape to promote flow attachment over the front of the plate, while the trailing edge has a single-sided taper (Fig. 1(*b*)). The taper is oriented to force flow separation on the side opposite the bubbles to ensure the flow remains attached on the side of the plate with the bubbles, and that measured changes in drag are due to changes in shear stress, not movement of a separation point. A row of boundary layer trips is adhered approximately 64 mm from the leading edge on both sides of the plate to generate turbulent boundary layer flow over the surface.

The plate may be mounted in either a horizontal or vertical configuration. The plate is suspended horizontally in the test section by four thin struts. In order to examine flow over large bubbles, thin strips of styrene are adhered to the sides of the bottom of the flat plate surface to form a large, shallow cavity. The plate is positioned cavity-side down in the middle of the test section, and air is injected into the cavity forming a large hydrostatically stabilized bubble on the bottom surface (Fig. 2). To instead examine flow over a solid flat plate, three flat aluminum plate inserts are screwed into the main-plate cavity to form a smooth solid flat plate surface.

Surface tension forces hold the tiny bubbles fixed to the TBA surface regardless of plate orientation. Thus, flow over tiny

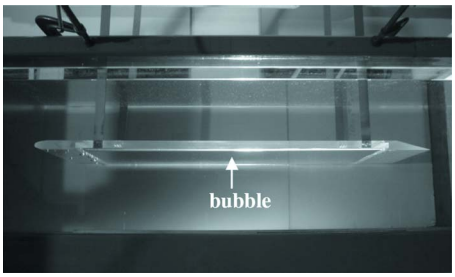

Fig. 2 Acrylic plate with large trapped bubble mounted horizontally in the test section

trapped bubbles is examined for a plate suspended vertically. The plate is suspended vertically by two flexures within fairings (Fig. 3). The remaining exposed flexure contributes a small drag; this additional drag as well as drag due to the boundary layer trips is included in the predicted one-seventh power law drag values presented in Sec. 3.3. Specifically, the analytic one-seventh power law profile represents a calculation of the drag assuming friction drag in the laminar flow up to the trips (D_{laminar}), a one-seventh power law velocity profile aft of the trips ($D_{\text{turbulent}}$), a profile drag contribution from the trips themselves (D_{trips}), and a profile drag contribution from the small area of the flexures exposed to the flow (D_{flexure}). The sum of these four drag contributions provide the drag estimate referred to as the analytic one-seventh power law for the flat plate. In particular, drag on the leading edge portion of the plate up to the trips is calculated assuming a Blasius solution

$$D_{\text{laminar}} = 2b\left(\frac{1}{2}\rho U_\infty^2\right)\frac{2 * 0.664 x_{\text{trips}}}{\sqrt{\frac{\rho U_\infty x_{\text{trips}}}{\mu}}} = 0.1514 U_\infty^{3/2} \tag{1}$$

where b is the plate span, x_{trips} is the streamwise location of the trips from the plate leading edge, ρ and μ are water density and dynamic viscosity, respectively, and U_∞ is the freestream flow speed. The drag on the turbulent flow region of the plate is given by

$$D_{\text{turbulent}} = 2\int_{x_{\text{trips}}}^{L} 0.0576\left(\frac{U_\infty x}{v}\right)^{-1/5}\left(\frac{1}{2}\rho U_\infty^2\right) b dx = 1.56 U_\infty^{9/5} \tag{2}$$

The drag due to the 60 boundary layer trips may be roughly approximated by

$$D_{\text{trips}} = 60 * C_D \tfrac{1}{2}\rho U_\infty^2 A = 0.15 U_\infty^2 \tag{3}$$

where A is the frontal area of each trip and $C_D \approx 0.5$ [16]. Finally, the majority of each flexure is shielded from the flow by the fairings, except for a 15-mm section. The drag on the exposed area is approximated by

$$D_{\text{flexures}} = 2 * C_D\left(\tfrac{1}{2}\rho U_\infty^2\right) A = 0.177 U_\infty^2 \tag{4}$$

where $C_D \approx 0.5$ [16] and $A \approx 1.5 \times 10^{-4}$ m^2 is the frontal area of each exposed flexure. The total analytic drag (in Newtons) is then

$$D_{\text{total}} = 0.1514 U_\infty^{3/2} + 0.327 U_\infty^2 + 1.56 U_\infty^{9/5} \tag{5}$$

The TBA is made of two 0.254 m $\times$ 0.381 m $\times$ 1.5875 mm aluminum plate inserts screwed into the acrylic plate cavity. These plate inserts are 6061 aluminum, polished with a Scotch Brite pad, degreased with acetone and treated with Metal Ready® primer, then airbrushed with a waterproof, nonconductive POR-15® Hardnose two-component epoxy coating. Small nonthru holes are drilled into the painted plates, comprising the cavities in which the trapped bubbles are formed. The drilling process exposes the conductive aluminum surface beneath, resulting in a flat plate surface with 367,000 holes m^{-2}. The holes are 1.143 mm in diameter and are drilled 0.762 mm into the aluminum plate in a staggered pattern. The bubble array begins at a location $x=0.127$ m, with $x=0$ being the location of the acrylic flat plate leading edge. At the highest Reynolds numbers examined, these holes are small; the hole diameter is about 21 viscous length scales (k^+) near the leading edge of the bubble region and 19 k^+ at the trailing edge. Since approximately 70% of the drag occurs over the leading 50% of the plate length, the two drilled plates are mounted closest to the leading edge, and a third simple painted plate is positioned downstream of them. Bubbles are produced in the drilled holes via electrolysis (Fig. 4). The conductive bubble plates are connected to the negative terminal of a power supply and thus work as the cathode and a nearby submerged stainless steel mesh is connected to the positive terminal and serves as the anode.

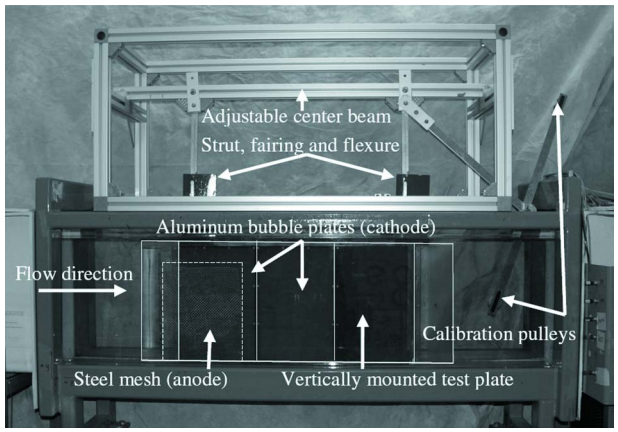

Fig. 3 Vertically mounted plate in the water tunnel test section. Test plate, cathodes, and anode are outlined for clarity.

2.3 Drag Measurement Systems. Drag measurements on the flat plate are obtained using either a proximity sensor/force balance system or by using a laser Doppler anemometer wake survey and momentum balance approach. Both measurement techniques may be used to obtain data for a vertically oriented plate, but drag on the horizontally mounted plate must be acquired using the LDA system. Bench tests of the proximity sensor, which measures the deflection of the aft support flexure (Fig. 5) showed repeatability of measurements to within 0.5% and negligible drift in voltage output over time.

The sensor signal is related to drag by a simple calibration

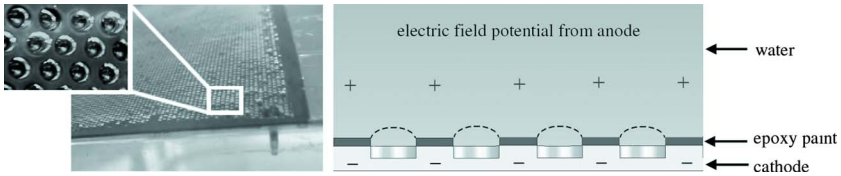

Fig. 4 Photograph of TBA during electrolysis (left). Schematic of the electrolysis process for trapped-bubble formation (right).

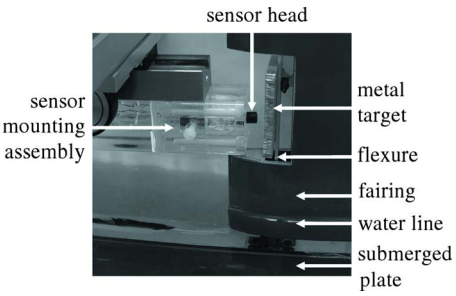

Fig. 5 Proximity sensor setup used in force balance measurements

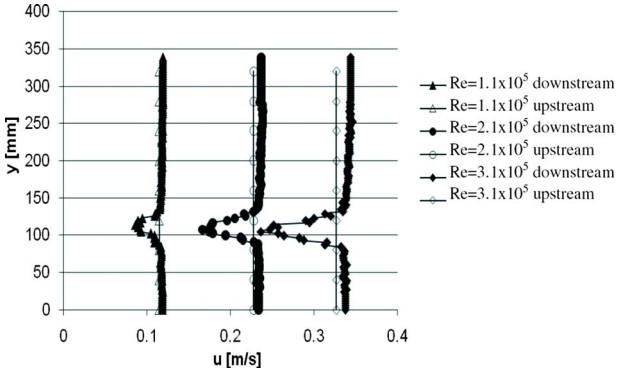

Fig. 6 Sample velocity profiles acquired at upstream and downstream stations of a horizontally mounted plate

technique as follows: the sensor head is positioned at its neutral value (which is equivalent to an output of 1.0 V $\pm$ 0.05 V) so that it is nearly touching the target. Six weights (0.016 kg each) are then hung in succession on a calibration fiber that is attached to the plate through a pair of pulleys shown in Fig. 3. The sensor is mounted such that the full load of calibration weights produces a deflection corresponding to the full-scale voltage output of the sensor, or approximately 11.0 V $\pm$ 0.05 V. The flexure deflection corresponding to this full-scale output is more than the maximum deflection occurring during the experiments. As the plate is displaced, the sensor output is sent to the computer and a LABVIEW virtual instrument (VI). The calibration curve fits were determined to be repeatable to within 10% (due to friction within the pulley system), which for a direct comparison of bubbles/no bubbles configurations is too large of a variation to be useful, as this trapped-bubble drag reduction method being tested is anticipated to produce up to a 10% drag reduction. Since the pulley system introduced additional error in the system that is not present during the experiments, one single calibration curve is instead acquired at the beginning of each set of experiments (one set consists of drag measurements taken over a range of Reynolds numbers with and without bubbles) and is used to compute an absolute drag for the entire set of experiments. Prior to each individual experiment, the vertical plate is prepared and the system is allowed to come to rest completely. Then the proximity sensor is set to its neutral value, and the voltage output by the proximity sensor during the experiments are converted to a force via the calibration curve.

Each drag value obtained using the proximity sensor is an average of ten individual measurements acquired in two sets of five in-test repeated measurements. The experimental procedure to obtain these measurements is as follows:

(1) Flat plate is prepared for experiment. If measuring drag without bubbles, all bubbles are removed from holes (by brushing over holes repeatedly with a small brush); if measuring drag with bubbles, bubbles are grown in holes via electrolysis, as described in Sec. 2.2 (holes are "full" when bubbles are protruding, as illustrated in Fig. 4).
(2) System is brought to rest and proximity sensor is set to its neutral value.
(3) Water tunnel is brought up to test speed and one drag measurement is then acquired every minute for 5 min. Each drag measurement is an average of 1000 samples acquired over 10 s at a sampling rate of 100 Hz, which yields approximately four statistically independent data points per acquisition. Freestream velocity measurements are also obtained during each experiment using the LDA.
(4) Water tunnel is turned off and system is brought to rest. The results from the experiment are accepted if the neutral value to which the sensor returns has not changed by more than 2% ($\pm$0.02 V) and rejected otherwise.
(5) Steps (3) and (4) are repeated a second time for the second set of in-test measurements.

The final goal of the experiments is to determine a relative change in drag produced by the TBA with and without bubbles. Error bars are calculated for the uncertainty in measured drag from the proximity sensor and also for the uncertainty in the corresponding Reynolds number.

The uncertainty in the sensor system is determined by measuring the variation in the proximity sensor neutral value before and after the experiment. The student's t-distribution is then used to calculate the contribution of this error to the overall uncertainty in the measured drag. The relative uncertainty in the sensor neutral value varied among experiments but is always equal to or less than 2.1% of the proximity sensor neutral value. Uncertainty is also dependent upon the random error in the experiments, which is calculated from the variation in the ten individual measurements using the student's t-distribution; uncertainty due to randomness in the experiments is always less than 4.1%. These two uncertainties added together determine the overall uncertainty in the drag measurements. These total uncertainties are generally around 2–3% of the measured drag value with the largest relative uncertainty being 6.64% of the drag value at the lowest Reynolds number tested. Since we are concerned with the relative change in drag between the two cases (flat plate drag with bubbles versus without bubbles), it is assumed that obtaining a sufficiently small uncertainty (using a 95% confidence level) in the sensor's neutral value plus random experimental uncertainty provides a standard through which we may compare the two drag values. As can be seen from Sec. 3.3, these measures of uncertainty are sufficient for determining whether we obtain the expected drag reduction using the TBA. A complete description of the uncertainty analysis is provided in Appendix C of Ref. [19].

Flat plate drag measurements for a vertically or horizontally mounted plate may be independently obtained by integrating the momentum equation over a control volume surrounding the test plate. When the plate is mounted horizontally in the test section, LDA velocity profiles must be obtained in the vertical y-direction to capture the wake profile. The upstream and downstream velocity profiles (Figs. 6 and 7) were obtained at the plate midspan and were numerically integrated assuming spanwise uniformity to obtain the total drag on the plate.

Comparison of the upstream and downstream velocity profiles shows a small streamwise flow speed increase along the plate due to solid blockage from the plate itself as well as wake blockage. This flow speed increase acts to slightly "pull" the model downstream. Corrections may be made for both types of blockage and are outlined according to Barlow et al. [14] below.

The correction for solid blockage is given by

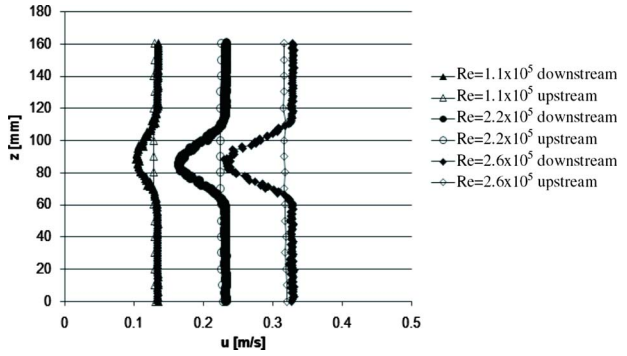

Fig. 7 Sample velocity profiles acquired at upstream and downstream stations of a vertically mounted plate

$$\varepsilon_{sb} = \frac{K_1 V_{model}}{C^{3/2}} \tag{6}$$

A parameter value of $K_1=0.74$ is suggested for the plate in the horizontal orientation and $K_1=0.52$ for the plate in the vertical orientation [14]. The variables V and C are plate volume and test section cross-sectional area, respectively. The solid blockage correction term was found to be approximately $\varepsilon_{sb}=0.077$.

The correction for wake blockage is given in Ref. [14] as

$$\varepsilon_{wb} = \frac{c}{4h} C_{du} \tag{7}$$

The parameter c represents the plate chord length, h is the water height (or channel span, as appropriate), and C_{du} is the uncorrected drag coefficient. The wake blockage correction was found to be approximately $\varepsilon_{wb}=0.011$ at the highest flow speeds. The uncorrected drag coefficient is determined by applying Eq. (8) to the control volumes. The wake width $Y_w=y_2-y_1$ is determined from the downstream velocity profile, and q and q_o are the dynamic pressures determined from the wake and downstream freestream velocity, respectively. Note that extending the numerical integration from Eq. (8) outside of the wake provides little to no contribution to the drag coefficient (since $q(y)$ is equal to q_o outside the wake); thus, the drag coefficient may be determined by numerically integrating Eq. (8) across the wake only

$$C_{du} = \frac{Y_w}{c} - \frac{1}{q_o c}\int_{y_1}^{y_2} q(y)dy \tag{8}$$

The solid and wake blockage corrections are applied to the uncorrected drag coefficient to yield the final drag coefficient value

$$C_d = C_{du}(1 - 3\varepsilon_{sb} - 2\varepsilon_{wb}) \tag{9}$$

from which we may obtain the drag. Note that the largest wake and solid body correction made to any of the drag coefficients was $C_d/C_{du}=0.74$ or about 26%.

3 Trapped-Bubble Results

3.1 Overview. We first examine the drag reduction produced by a large trapped bubble on the bottom of the horizontally mounted flat plate. Results from these large trapped-bubble experiments provide some perspective on the characteristics of the tiny trapped bubbles, which are significantly more difficult to study to the extent of that done for the large bubble. In particular, bubble surface contamination observed on the large trapped bubble is found to correspond to the amount of drag reduction obtained, and it is expected that this observation will apply for the tiny trapped bubbles. Drag results from this study also provide insight into the magnitude of maximum drag reduction attainable by a trapped-bubble drag reduction method.

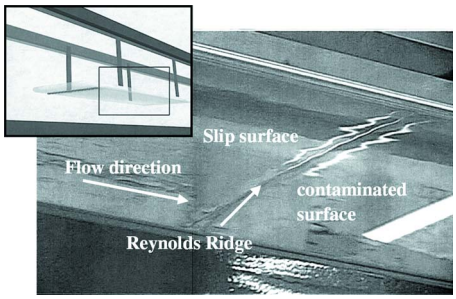

Fig. 8 Reynolds ridge formation on the surface of a large trapped bubble. Note that the Reynolds ridge is nearly straight and spans virtually the entire bubble width. View taken from an oblique angle below bubble (see schematic).

3.2 Large Trapped-Bubble Results. Several interesting bubble surface phenomena were observed on the large bubble. After forming the large bubble in the cavity, contaminants in the water accumulate onto the clean bubble surface over time. When the flow is turned on, shear forces strip away some of these contaminants while the rest are pushed toward the back of the bubble, resulting in a bubble, which has a clean surface in front and a contaminated surface further downstream.

A crease in the surface separating these two regions of clean and contaminated bubble surface is known as the Reynolds ridge (Fig. 8). These regions were examined by using the LDA to acquire streamwise mean and rms velocity profiles near the surface of the bubble (Fig. 9). The mean velocity profile acquired at the surface of the contaminated region (at a location $x=0.323$ m downstream of the leading edge) shows a large velocity gradient at the bubble surface with only a small slip velocity, which is approximately 10% of the freestream value.

It is believed that the relatively large velocity gradient at the interface is caused by the build-up of contaminants at the surface. A small amount of velocity slip is observed, which may be a result of the movement of the contaminants on the bubble surface. The

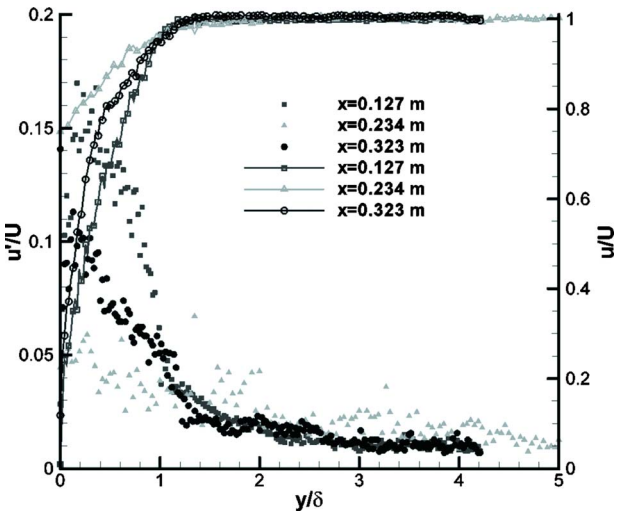

Fig. 9 Streamwise mean (line with open symbols) and rms (filled symbols) velocity profiles acquired over a large trapped bubble at three streamwise locations from $y/\delta=0$ ($y=0$ mm, on the surface) to $y/\delta=5$ ($y=20$ mm) with $U_\infty=0.17$ m/s, where δ is based on $0.95U_\infty$. Measurements taken at $x=0.127$ m from the leading edge correspond to the solid flat plate surface, $x=0.234$ m corresponds to the clean portion of the trapped bubble, and $x=0.323$ m corresponds to the contaminated portion of the trapped bubble (approximately 3 cm downstream of the Reynolds ridge).

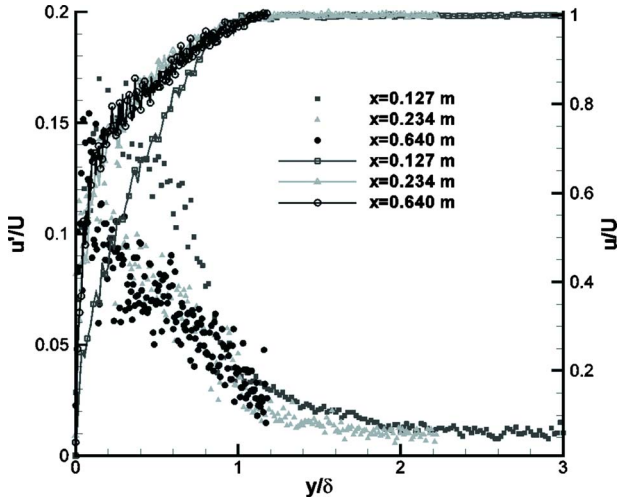

Fig. 10 Streamwise mean (line with symbols) and rms (filled symbols) velocity profiles acquired over a solid flat plate surface at three streamwise locations from $y/\delta=0$ (surface) to $y/\delta=3$ with $U_\infty=0.17$ m/s, where δ is based on $0.95U_\infty$. Measurements taken at $x=0.127$ m are identical to the data set presented in Fig. 9. Measurements at $x=0.234$ m correspond to the second measurement location in Fig. 9, $x=0.640$ m corresponds to the end of the trapped-bubble array.

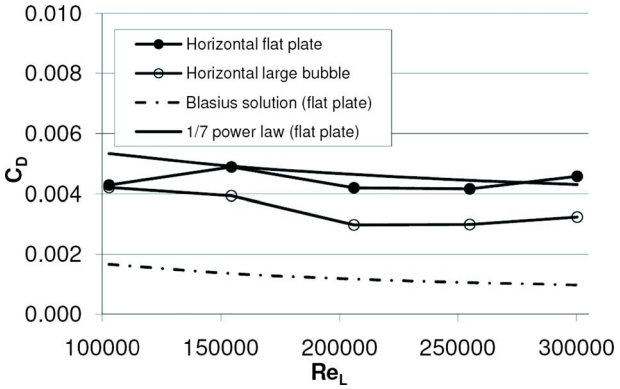

Fig. 11 Drag profiles obtained by the LDA wake survey over a range of Reynolds numbers based on plate length ($1.1\times10^5<\mathrm{Re}_L<3.1\times10^5$) for a horizontal flat plate and a horizontal plate with a large trapped bubble. The one-seventh power law solution accounts for laminar flow up to the boundary layer trips, drag due to the trips and turbulent flow downstream of trips.

streamwise rms velocity does not go to zero at the surface of the contaminated bubble region, shown by the circle symbols in Fig. 9, perhaps because this surface is not rigid and the air allows for compliance at the interface. The contaminants formed a visible crust on the bubble surface that exhibited slow, large-scale convection within the contaminated layer like that discussed previously by Phongikaroon et al. [15]. However, the mean velocity profile at $x=0.234$ m shows that the clean portion of the bubble exhibits near-slip at the surface; the clean bubble surface velocity was approximately 85% of the freestream value, thus the velocity gradient (and therefore shear stress) at the bubble surface was relatively small. Similar to the contaminated bubble surface, we observe from the triangle symbols in Fig. 9 that the rms velocity reaches its peak value at the clean bubble surface. It is interesting to compare this peak rms velocity value on the clean bubble surface to what we observe for the peak rms velocity at the same x-location, but on a solid surface (Fig. 10); the peak rms velocity on the clean bubble surface is approximately one-half the peak rms velocity value of a tripped boundary layer developed over a solid surface. At the lowest Reynolds number tested, the Reynolds ridge was noted to be located 0.27 m behind the leading edge of the bubble. As flow speed increased and shear at the bubble surface became greater, the fraction of the contaminated region of the bubble became progressively smaller; high shear pushed the surface contaminants further back on the bubble surface, resulting in a larger region of slip surface on the front of the bubble (Table 1). This is consistent with the observations in Ref. [6]. In their study, continuous air injection was used to form a presumably uncontaminated air layer on the bottom surface of the flat plate, resulting in 100% drag reduction on the solid surface shielded by the air layer. The uncontaminated region of the bubble in the current experiments indicate the same level of drag reduction as achieved in the high Reynolds number experiments of Sanders et al. [6].

Table 1 Reynolds ridge location and corresponding drag reduction for large trapped bubble

Re_L	Reynolds ridge location (m)	Percent slip on plate surface (%)	Percent drag reduction (%)
1.1×10^5	0.27	13	−3
1.6×10^5	0.47	23	19
2.1×10^5	0.58	29	29
2.6×10^5	0.68	34	27
3.1×10^5	0.71	35	32

Figure 10 shows similar mean and fluctuating velocity profiles taken at three streamwise (x) locations on the solid top side of the plate for comparison. The profiles on the top solid surface clearly indicate a turbulent boundary layer that is not fully developed at these Reynolds numbers. The first streamwise mean velocity profile at $x=0.127$ m (shown by a line with square symbols) in Fig. 10 reflects the wake of the boundary layer trips. A fully developed canonical turbulent boundary layer is, of course, not expected in such a regime and so close to the trips, but for our purposes it is not required either as we are simply running a side-by-side direct comparison to determine if a large bubble or TBA can reduce viscous drag. Farther downstream at $x=0.234$ m and $x=0.640$ m, we see the boundary layer thickening and the normalized streamwise rms velocity peak values approaching 0.11–0.12, which is approximately what we would expect to see in a canonical turbulent boundary layer [16].

The values for the drag coefficient obtained from both a simple solid horizontal flat plate and horizontal plate with a large trapped bubble are shown in Fig. 11. Note that the values agree closely with the analytic flat plate drag coefficient value for turbulent flow aft of the trips, rather than the laminar Blasius solution. In drag coefficient values presented, blockage effects are accounted for as indicated above in Sec. 2.3, but no accommodation is made for the edge effects of the plate near the sidewalls or the free surface. Introducing a large trapped bubble on the bottom surface of the plate significantly reduces the drag on the flat plate. Moreover, the percent drag reduction improves with increasing Reynolds number (Table 1), which corresponds to the movement of the Reynolds ridge further aft along the bubble surface and the increase in percent of slip on the plate surface. In fact, there is good agreement between the percent slip on the bubble surface and the percent drag reduction obtained. In Table 1, the ridge location refers to the downstream distance from the leading edge of the bubble. The percentage of slip is calculated as the ratio of the plate surface covered by clean bubble to the total wetted surface area of the flat plate. The percent drag reduction refers to the percent change in total drag per unit span of the flat plate with a large trapped bubble compared with the simple flat plate case. It should be mentioned that the difference in drag measured at the lowest Reynolds number for the flat plate and large trapped-bubble case is expected to be within the experimental uncertainty of the measurement; thus,

the drag reduction calculated at this particular Reynolds number is not considered to be reliable. We have observed that the plate with the large bubble, when left in the flow for several hours, builds up contamination on the surface and the Reynolds ridge moves forward, but we have not measured drag changes over long times. Presumably, the drag would increase as the amount of clean bubble is reduced.

While the use of a large bubble for drag reduction in a practical case seems unlikely, the bubble did generate some remarkable flows. Dye was injected with a needle into the flow just upstream of the bubble, and some of the dye became entrained in the air-water interface. It was rapidly swept off of the clean region and accumulated on the contaminated surface, forming streamwise streaks. The dye, along with the visible surface contaminants, highlights both large and small scale secondary flows on the bubble surface. These flows appear reminiscent of those observed by Phongikaroon et al. [15] in which a pair of recirculation cells was seen in a much smaller apparatus. The Reynolds ridge on our relatively large bubble spanned straight across the bubble surface. Spanwise-periodic fingerlike recirculation regions appeared in the surface contaminants reflecting both upstream- and downstream-moving flow on the interface. Hence, it appears that Phongikaroon et al. [15] were observing a single mode viscous instability of the contaminated interface while in our larger channel we obtain a multimode recirculating flow. That is, the small slip condition on the contaminated interface (Fig. 9) is a result of a time average over these up/downstream moving recirculation regions.

The drag reduction from the large trapped bubble presented in this paper should be comparable to the near 100% drag reduction obtained from the quasi-continuous bubble film by Sanders et al. [6]; however, it must be emphasized that the measurement technique used herein is different. Sanders et al. [6] considered only drag reduction on the bottom portion of the flat plate, and drag reduction was obtained by acquiring six local skin friction measurements along the length of the plate. In the present study, the total drag on the plate is measured using an LDA wake survey momentum integration technique, which obtains a measurement of total drag per unit span. The technique used in Ref. [6] was sensitive to the location of the gas film on the plate surface, particularly when the film was quasi-continuous. For example, a quasi-continuous bubble forming around (not over) the strain gage sensors may indicate a smaller drag reduction than actually exists on the bottom of the plate, while a gas film forming over only the sensors may indicate a larger drag reduction than actually exists. Thus, the large trapped-bubble drag reduction measurements reported in the present paper may not correspond to those obtained by Sanders et al. [6].

The observations, measuring techniques and drag reduction results obtained from the large bubble study offer both encouraging and useful information leading up to the drag reduction study using a TBA. However, it is not obvious how a Reynolds ridge applies to tiny bubbles. It is expected that contaminants found in the water will accumulate on the tiny bubble surfaces but may be stripped away or pushed to the back of the bubble surface similar to the large bubble. We do not expect that there would be any complex viscous recirculating flows on such tiny bubbles; one might expect at most a simple pair of recirculation cells. However, we did not directly observe this phenomenon on the tiny bubbles; it would be difficult to see due to their small size.

3.3 Trapped-Bubble Array Results. The tiny trapped bubbles offer more versatility than large bubbles in the experimental process and perhaps in applications in the sense that, due to a relatively greater influence of surface tension, tiny bubbles are more hydrodynamically stable than the large bubble. To demonstrate this, the test plate was mounted vertically in the test section in anticipation of demonstrating the drag-reducing capabilities of this method. For the flow speeds examined in these experiments, the largest bubbles in the trapped-bubble array have capillary and Reynolds numbers on the order of 10^{-3} and 10^{2}, respectively, which are defined as

$$\mathrm{Ca}_d \equiv \mu_{\mathrm{liquid}} \left.\frac{\partial u}{\partial y}\right|_{\mathrm{wall}} \frac{d}{\sigma} \tag{10}$$

$$\mathrm{Re}_d \equiv \frac{\rho \left.\frac{\partial u}{\partial y}\right|_{\mathrm{wall}} d^2}{\mu_{\mathrm{liquid}}} \tag{11}$$

Here, d is the bubble diameter and σ is the surface tension. Numerical studies by Feng and Basaran [17] on two-dimensional cylindrical bubbles indicate that the bubbles sizes used in our experiments are within the critical Reynolds number limit: full-profile bubbles at the bubble plate leading edge and highest test speeds have a Reynolds number and capillary number of $\mathrm{Re}_{d,\mathrm{turbulent}} \cong 239$ and $\mathrm{Ca}_{d,\mathrm{turbulent}} \cong 0.0043$, while Ref. [17] report that $\mathrm{Re}_c = 243.7$ for $\mathrm{Ca} = 0.005$ corresponds to neutral stability of the two-dimensional bubble surfaces. The product of the capillary and Reynolds numbers would yield a Weber number that, in this case, is approximately unity suggesting only small bubble deformations. Presumably in higher speed, higher shear stress flows, the bubble diameter would have to be reduced appropriately to maintain bubble stability.

It was noted during the experiments using the TBA that high shear at the plate surface tended to tear away the larger bubbles protruding from the surface at higher Reynolds numbers. The largest protruding bubbles were stripped away at the highest Reynolds number tested, resulting in a TBA with approximately 75% bubble coverage. This suggests that drag reduction, if it could be obtained, may diminish at higher flow speeds unless lost bubbles are actually replaced by electrolysis. We note that drag measurements were obtained with electrolysis power off: the bubbles were created before the test only in order to avoid having the stainless steel anode mesh in the test section during the experiments as it produced a large displacement thickness and increased the measured drag on the plate.

Drag measurements were obtained over a range of Reynolds numbers based on plate length, L ($7.2 \times 10^4 < \mathrm{Re}_L < 3.1 \times 10^5$) for both a vertical plate without trapped bubbles and a vertical plate filled with trapped bubbles. The drag on the vertically mounted plate is measured using both the proximity sensor measurement system and by a wake survey for the two cases examined. In both cases, the same three plate inserts remained in the cavity: two drilled bubble plate inserts in the front and one simple flat plate insert in the back. At the highest Reynolds numbers examined, the hole diameter is about 21 viscous length scales k^+ near the leading edge of the bubble region and 19 k^+ at the trailing edge. Although the holes themselves do not protrude into the flow, the surface is expected to be transitionally rough [16,18]. While we could have compared the drag of a TBA plate to a simple smooth plate it is reasonable to believe that (1) the holes in the bubble plates were sufficiently small so as to have only minor effects on the plate drag and (2) as seen below, the presence of bubbles in the holes hardly affected the drag so it did not matter. The drag results for each case are plotted in Fig. 12; open square and closed triangle symbols correspond to the proximity sensor measurements with and without bubbles, respectively, and are observed to be higher than the analytic (one-seventh power law) turbulent solution.

This difference in drag as measured by the proximity sensor and the wake survey may be a result of the uncertainty in the calibration curve fit discussed in Sec. 2.3, but it is also important to note that the drag values are obtained using two fundamentally distinct measurement techniques on a finite span plate. Measurements using the proximity sensor are obtained from a resultant displacement of the plate due to the total physical drag force on the plate, which presumably includes additional drag due to plate end effects. LDA velocity measurements across the span of the

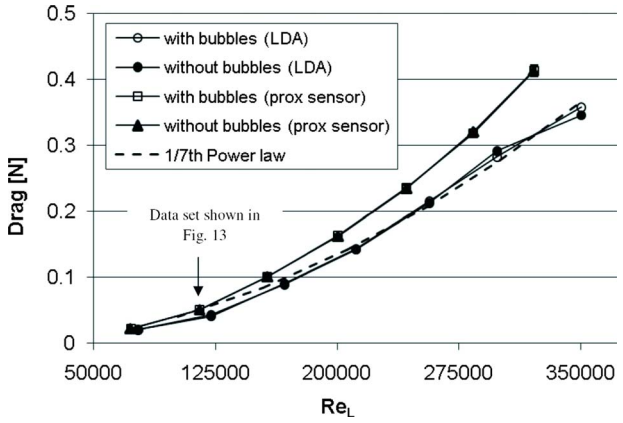

Fig. 12 Drag measurements obtained for a vertical flat plate ($7.2\times10^4<Re_L<3.1\times10^5$) with and without trapped bubbles using LDA and proximity sensor measurement systems. The one-seventh power law solution accounts for laminar flow up to the boundary layer trips, drag due to the trips and turbulent flow downstream of trips, and drag contributions from flexures (for vertical plate case). Error bars (based on a 95% level of confidence) are included for the proximity sensor data but are very small.

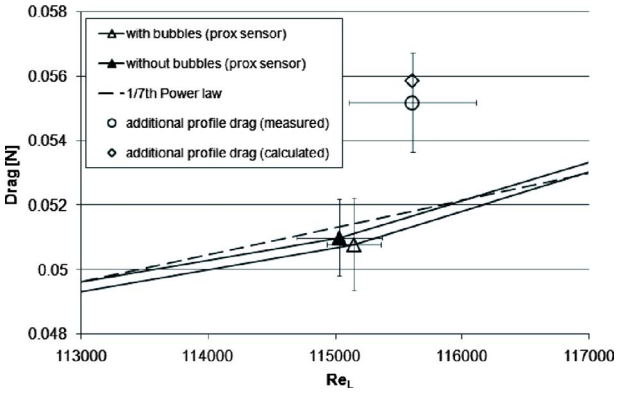

Fig. 13 Detailed plot of proximity sensor drag measurements (triangle symbols) corresponding to $Re_L=1.15\times10^5$ from Fig. 12. Error bars are based on a 95% level of confidence. Circle symbol shows 7.8% increase in drag due to an additional roughness element affixed to the plate in comparison to a calculated 9.8% drag increase seen with the open diamond symbol.

plate indicate that disturbances due to plate end effects spread toward the plate centerline at a streamwise spreading angle of approximately 11 deg. Drag measurements using the wake survey are obtained from velocity profiles taken at the plate midspan location, which should not reflect strong plate end effects, resulting in a lower measured drag compared with the force balance measurements. The disturbances and perhaps weak vortices forming in between the plate, channel floor, and free surface or weak free surface wave drag should be expected to lead to a higher drag than would occur for an infinite span flat plate.

The area of the flat plate covered with tiny trapped bubbles accounts for only 8.66% of the total wetted surface of the plate, so the effect of the trapped bubbles on the measured drag is expected to be small. Uncertainties in measured drag values ranged from approximately 1.1% to 6.6%, and uncertainties in measured Reynolds numbers were all within 0.5%. These uncertainty error bars are included on the proximity sensor data in Fig. 12, but are small compared with the symbols shown. Drag measurements (with and without bubbles) obtained from the proximity sensor at $Re_L=1.1\times10^5$ are shown in detail in Fig. 13.

Over the range of Reynolds numbers examined, all drag measurements with and without bubbles lie within the experimental uncertainty, so no substantial drag reduction was observed with the TBA. To demonstrate that the proximity sensor system is in fact able to measure a small change in drag (particularly at the low Reynolds numbers where we are trying to measure small changes in small drag values), three roughness elements were attached to the side of the plate in a separate experiment. Each roughness element was a simple rectangular aluminum shim. The elements were inserted lengthwise in the narrow gap between the first and second bubbles plates such that they were protruding from the plate surface, with 2.0 cm $\times$ 0.5 cm wetted frontal areas. The expected drag due to these three roughness elements was calculated based on the drag on a rectangular plate (with a drag coefficient, $C_D=2$) in freestream flow for $Re_L=1.15\times10^5$. The calculated percent drag increment due to this added roughness element is approximately 9.8%. The actual measured drag value is expected to be slightly smaller than this value since a significant portion of the roughness element is within the boundary layer of the plate. The drag measurements obtained from this study are shown in Fig. 13. It can be seen in the figure that the roughness elements increase the drag measured on the flat plate by approximately 0.004 N, which corresponds to a 7.8% drag increase in close agreement with the calculated 9.8%.

Drag measurements were also obtained using the numerical integration of the LDA wake survey and are shown in Fig. 12 as well. The open circle symbol corresponds to flat plate drag with bubbles, and the closed circle corresponds to a flat plate without bubbles. Both of the trends obtained from the LDA measurements agree remarkably well with the predicted (analytical) drag curve for a solid flat plate. Uncertainty analysis was not performed on the data obtained from the LDA as only one full velocity profile was obtained for each test case at each Reynolds number, but the percent changes in drag obtained from the LDA measurements again indicate negligible drag reduction from the TBA.

4 Summary and Conclusions

The principle objective of this experimental program was to demonstrate the drag-reducing capabilities of the TBA drag reduction approach, although no drag reduction was found. A baseline set of experiments involving a large trapped bubble provided a source of comparison and observations to examine the underlying principles of the TBA drag reduction approach, and provided insight as to the maximum drag reduction one could hope for with the trapped-bubble method.

Drag results for the trapped-bubble experiments were obtained using two independent measurement techniques: a proximity sensor, which measured plate deflection of the aft supporting flexure, and a wake survey using a LDA system. Drag measurements were acquired for a horizontally oriented solid flat plate and a horizontally mounted plate with a large trapped bubble on the bottom surface. Drag measurements were also acquired for a vertically oriented plate with bubble plate inserts that were either bare or filled with bubbles.

The large trapped bubble produced a maximum drag reduction of 32%, corresponding to a slip area, which occupied 35% of the wetted plate surface. The large trapped bubble indicated an improved drag reduction with increasing Reynolds number, which is believed to be a result of the slip surface increase associated with the receding Reynolds ridge on the bubble surface. Thus, it is reasonable to suggest that a clean bubble surface provides a drag reduction roughly proportional to the wetted surface area, which it occupies. This may also provide insight as to why no drag reduction was observed using the TBA; the means of bubble formation in each of the two experiments are significantly different. Recall that air is injected into the bottom-facing cavity of the plate to form the large trapped bubble, while electrolysis is used to form the TBA. It was observed during experiments that a white precipi-

tate (presumably a by-product of electrolysis) formed and collected inside the tiny bubble cavities over time. It is possible that this precipitate, although difficult to see due to the small size of the bubbles, collects on the surfaces of the tiny bubbles, effectively forming a no-slip bubble surface and inhibiting slip.

The tiny trapped bubbles that constituted the TBA surface covered only 8.66% of the wetted plate surface. The uncertainty analysis revealed that the change in drag observed from TBA measurements was within the experimental uncertainty and was not close to 8.66%. Thus, no appreciable drag reduction was obtained using the current trapped-bubble array method. No uncertainty analysis was performed for the LDA measurements, but the percent changes in drag generally agreed with the results obtained using the proximity sensor measurement system. Hence, it is not possible to make a claim of drag reduction using the TBA with any reasonable certainty and a cost/benefit analysis for use of a TBA is inappropriate.

Future work on the TBA concept should examine in greater detail flow over the tiny bubble surfaces in order to determine to what extent surface contaminants (either from the tap water or from the electrolysis process) affect slip on the bubble surface. It is possible that the tiny bubble surface behaves differently (in comparison to the large trapped bubble) when contaminated, and it is not clear whether a Reynolds ridge forms on the tiny bubble surfaces. Nonetheless, if the tiny bubbles provide clean slip surfaces, it would be important to investigate in detail the flow field over the TBA to determine if mean velocity slip occurs. In addition, bubble parameters including size and configuration should be investigated, and means of producing smaller holes should be sought. The Computer Numerical Control (CNC) machining process used here required approximately 2 s of drilling time for each hole, which is approaching the tolerable manufacturing limit to produce an entire surface of these holes.

Acknowledgment

The authors would like to thank Dr. David Bogard from the Mechanical Engineering Department at the University of Texas at Austin for his suggestions. Also thanks to Rick Maldonado, Travis Crooks, Frank Wise, Pablo Cortez, and their supporting staff for their contributions to the design and manufacturing of hardware used in this research. This research was sponsored by the Texas Advanced Technology Program.

References

[1] Matveev, K. I., 2003, "On the Limiting Parameters of Artificial Cavitation," Ocean Eng., **30**(9), pp. 1179–1190.
[2] Latorre, R., 1997, "Ship Hull Drag Reduction Using Bottom Air Injection," Ocean Eng., **24**(2), pp. 161–175.
[3] Madavan, N. K., Deutsch, S., and Merkle, C. L., 1984, "Reduction of Turbulent Skin Friction by Microbubbles," Phys. Fluids, **27**(2), pp. 356–363.
[4] Madavan, N. K., Deutsch, S., and Merkle, C. L., 1985, "Measurements of Local Skin Friction in a Microbubble-Modified Turbulent Boundary Layer," J. Fluid Mech., **156**, pp. 237–256.
[5] Pal, S., Deutsch, S., and Merkle, C. L., 1988, "Bubble Characteristics and Trajectories in a Microbubble Boundary Layer," Phys. Fluids, **31**(4), pp. 744–751.
[6] Sanders, W., Winkel, E., Dowling, D., Perlin, M., and Ceccio, S., 2006, "Bubble Friction Drag Reduction in a High-Reynolds-Number Flat-Plate Turbulent Boundary Layer," J. Fluid Mech., **552**, pp. 353–380.
[7] Balasubramanian, A., Miller, A. C., and Rediniotis, O. K., 2004, "Microstructured Hydrophobic Skin for Hydrodynamic Drag Reduction," AIAA J., **42**(2), pp. 411–414.
[8] Joseph, P., Cottin-Bizone, C., Benoît, J. M., Ybert, C., Journet, C., Tabeling, P., and Bocquet, L., 2006, "Slippage of Water Past Superhydrophobic Carbon Nanotube Forests in Microchannels," Phys. Rev. Lett., **97**(15), p. 156104.
[9] Ou, J., Perot, B., and Rothstein, J. P., 2004, "Laminar Drag Reduction in Microchannels Using Ultrahydrophobic Surfaces," Phys. Fluids, **16**(12), pp. 4635–4643.
[10] Reed, J. C., Bushnell, D. M., and Weinstein, L. M., 1991, "U.S. Patent for Hydrodynamic Skin-Friction Reduction," U.S. Patent No. 5,05,412.
[11] Stephani, K., and Goldstein, D., 2007, "The Effects of Trapped Bubbles on Viscous Drag Reduction for Submerged Surfaces," AIAA Paper No. 2007-4101.
[12] Stephani, K., Marr, K., Doctor, R. and Goldstein, D., 2006, "Drag Reduction Using Trapped Bubbles on a Flat Plate Surface," AIAA Paper No. 2006-3193.
[13] Goldstein, D., 2006, "U.S. Patent for Methods for Reducing the Viscous Drag on a Surface and Drag Reducing Device," U.S. Patent No. 7,044,073 B2.
[14] Barlow, J. B., Rae, W. H., and Pope, A., 1999, *Low Speed Wind Tunnel Testing*, 3rd ed., Wiley-Interscience, New York.
[15] Phongikaroon, S., Peter, J. K., Smith, G., and Handler, R., 2004, "The Thermal Structure of a Wind-Driven Reynolds Ridge," Exp. Fluids, **37**(2), pp. 153–158.
[16] White, F. M., 2006, *Viscous Fluid Flow*, 3rd ed., McGraw-Hill, New York.
[17] Feng, J. Q., and Basaran, O. A., 1994, "Shear Flow Over a Translationally Symmetric Cylindrical Bubble Pinned on a Slot in a Plane Wall," J. Fluid Mech., **275**, pp. 351–378.
[18] Schlichting, H., 1987, *Boundary-Layer Theory*, 7th ed., McGraw-Hill, New York.
[19] Stephani, K., 2006, "Drag Reduction Using Trapped Bubbles on a Submerged Flat Plate Surface," MS thesis, Department of Aerospace Engineering and Engineering Mechanics, University of Texas at Austin, Austin, TX.